Substrate effects on indentation plastic zone development in thin soft films

D.E. Kramer
Metallurgy Division, National Institute of Standards and Technology, Gaithersburg, Maryland 20899-8553

A.A. Volinsky
Motorola, DigitalDNA Labs, Process and Materials Characterization Lab, Mesa, Arizona 85202

N.R. Moody
Materials Reliability Division, Sandia National Labs, Livermore, California 94551-0969

W.W. Gerberich
Department of Chemical Engineering and Materials Science, University of Minnesota, Minneapolis, Minnesota 55455

(Received 5 January 2001; accepted 20 August 2001)

Plastic zone evolution in Al–2 wt% Si metal films on silicon and sapphire substrates was studied using nanoindentation and atomic force microscopy (AFM). AFM was used to measure the extent of plastic pileup, which is a measure of the plastic zone radius in the film. It was found that the plastic zone size develops in a self-similar fashion with increasing indenter penetration when normalized by the contact radius, regardless of film hardness or underlying substrate properties. This behavior was used to develop a hardness model that uses the extent of the plastic zone radius to calculate a core region within the indenter contact that is subject to an elevated contact pressure. AFM measurements also indicated that as film thickness decreases, constraint imposed by the indenter and substrate traps the film thereby reducing the pileup volume.

I. INTRODUCTION

The popularity of nanoindentation is due in large part to its ability to probe the mechanical properties of materials in a nondestructive fashion without extensive sample preparation. However, it is often difficult to measure film properties independent of the substrate properties. Several solutions to this problem have been proposed with varying degrees of success, the simplest being the "10% rule," by which it is proposed that the film properties can be measured for indentation depths less than 10% of the total film thickness.

However, this "rule of thumb" has several deficiencies. The rule is too restrictive for soft coatings on hard substrates;[1] it may not be restrictive enough for hard coatings on soft substrates; and the shape and size of the plastic zone are sensitive to indenter angle.[2,3] In addition, for submicron thick films, it can be experimentally difficult to perform and analyze indents that satisfy this requirement.

Other partially empirical approaches have attempted to incorporate the mechanical properties of the substrate into the hardness measurement through various rules of mixtures.[4–12] These generally express the composite hardness, H_c in the form:[13]

$$H_c = H_s + (H_f - H_s)\phi_H \quad , \tag{1}$$

where H_s and H_f are the hardness of the substrate and film, respectively, and ϕ_H is one of a variety of weighting functions depending upon the particular model.

For example, one common approach is to calculate plastic volumes based on the spherical cavity model developed by Hill[14] and adapted to the indentation process by Marsh,[15] Johnson,[16] and Chiang *et al.*[17] However, Ford has suggested that the work of indentation is related to indentation volumes and not plastic volumes.[18] In addition, the spherical cavity model does not describe the deformation process of a soft film on a hard substrate. The hard substrate has properties similar to a rigid half-space from the perspective of the film; thus, the case is better modeled by a slip-line field solution.[1,3]

Finite element studies (FEM) have provided additional insight into the indentation deformation process.[15,19–21] Studies of spherical indentation found formation of

pileup around the indenter, as well as hydrostatic regions at the indenter apex and the film–substrate interface.[19] Laursen and Simo[20] demonstrated how this pileup can have a significant effect on the measurement of hardness and modulus when accepted analysis methods are used.[22,23] This effect has also been observed experimentally.[24]

For films on the order of a micrometer or thicker, nanoindentation techniques provide an accurate method for determining thin film mechanical properties. However, for films from one to hundreds of nanometers thick and for indenter geometries deviating from the sharp conical indenters assumed in FEM simulations, tip–substrate interactions can have interesting effects on the deformation of thin films. For example, FEM simulations of sphero-conical indentation have shown that the magnitude of the indenter tip radius has little effect on contact pressure for indentation depths below half the film thickness.[25] However, for deeper indents, contact pressures gradually become greater for larger tip radii at the same penetration depth. It has also been demonstrated that as the size of the contact area increases with respect to the film thickness, material under the indenter experiences a state of hydrostatic stress.[19] This in turn convolutes the hardness measurement. While the pressure distribution under the indenter in the case of a confined thin film is experimentally indeterminate, the results of this constraint manifest themselves in the form of changes in the contact area and plastic zone.

While the plastic zone has been used in volume fraction models, as outlined above, few if any studies have been aimed at its direct measurement in thin film. Previous experimental investigations have shown that for materials with low strain hardening capacity, the extent of plastic pileup, as measured by atomic force microscopy (AFM) is in good agreement with the elastic–plastic boundary predicted by the spherical cavity model.[26,27] It is important to note however, that for materials with high strain hardening rates, sink-in is observed and AFM analysis cannot be used. Other studies of the plastic zone size using transmission electron microscopy[28,29] and dislocation etch-pits[30] also give comparable agreement with the spherical cavity model. In this study, AFM was combined with nanoindentation to measure the evolution of the plastic zone and contact radius for aluminum films on hard substrates. The evolution of the plastic zone was then taken as a measure of film constraint, and a model is proposed that incorporates this effect in a composite hardness analysis.

II. EXPERIMENTAL PROCEDURE

An Al alloy with a mass fraction of 0.02 Si (Al–2 wt% Si) was direct current (dc) sputter deposited to 340 nm, 500 nm, 1 μm, and 2 μm thickness on Si(001) wafers. Prior to deposition, each wafer was thermally oxidized to produce a 3-μm layer of SiO_2. In addition, Al–2 wt% Si was deposited onto Al_2O_3 (0001) substrates to 1- and 2-μm thickness. X-ray diffractometry showed the films to have a weak (110) texture with no preferred in-plane orientation. Nanoindentation tests were then conducted on the samples using a Nanoindenter II equipped with a 90° conical diamond indenter with a 700 nm radius of curvature at the tip. The choice of a 90° cone accentuates plastic pileup around the contact and eliminates corner effects found in Berkovich and Vickers indents thereby making surface profilometry measurements more precise. Each film was indented ten times at depths of 20%, 50%, 100%, and 120% of the total film thickness, with all indents spaced 100 μm apart. Contacts at lesser depths did not produce detectable plastic pileup, and the resulting hardness measurements showed a large amount of scatter. Figure 1 shows a series of load–displacement curves for a 2-μm-thick Al–2 wt% Si film on Si. The most severe indents were deep enough to cause appreciable plastic deformation of the substrate. Loading rates varied depending on film thickness and penetration depth according to the general procedure and loading rates outlined in Table I.

Each indent was then imaged using the contact AFM mode of a Digital Instruments 3100 scanning probe microscope. Contact areas were measured from the plan-view images based on peak pileup heights, from which the average contact radius *a* of each indent was determined [Fig. 2(a)]. Vertical sections from the surface profile were then taken at 45° intervals from which the extent of plastic pileup on both sides of the contact was measured [Fig. 2(b)]. The average of all four measurements determined the plastic zone diameter 2*c*. Potential

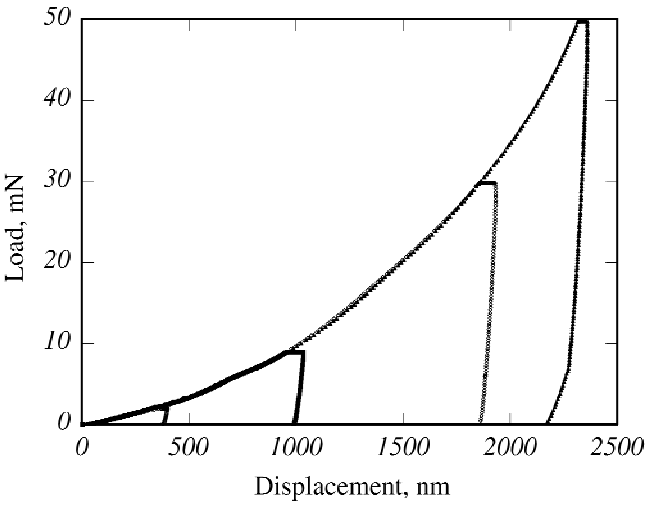

FIG. 1. Series of load–displacement curves into a 2 μm Al–2 wt% Si film on a silicon substrate. The indenter was a 90° cone with 700-nm radius spherical tip.

systematic errors in measurement of *a* and *c* were accounted for by measuring inner and outer limits of each and using the difference as the measurement error.

For the first 150 to 200 nm of indentation depth, the evolution of pileup and plastic zone in the film is determined by the geometry of the spherical portion of the tip and the film–substrate interface. Larger penetration depths are within the conical portion of the tip, which dictates further pileup and plastic zone development. In this study, the only indents within the spherical regime were for indentation depths below 50% of the film thickness in the 340 and 500 nm films.

III. RESULTS AND DISCUSSION

A. Experimental determination of thin film indentation deformation

Figures 2(a) and 2(b) show a plan-view contact mode AFM image and a cross section through this image taken from the 500-nm film on the Si substrate. The outer set of arrows in Fig. 2(b) mark the extent of the plastic zone measured from this cross section. The height of the pileup is about 20% of the indentation depth, in very good agreement with the finite element simulations[20] and other experimental observations.[24]

The hardness of each film was calculated using the load from the load–displacement curves and the projected contact areas measured from the AFM images.

TABLE I. Loading profiles used for all indents into Al–2 wt% Si films on Si and sapphire substrates along with typical loading rates and hold times for a shallow and deep indentation. All indents were performed using a 90° conical diamond indenter with a 700-nm tip radius.

Profile step	20% film thickness	120% film thickness
Linear load	10 μN/s	300 μN/s
Hold	60 s	60 s
Unload to 5% max load	10 μN/s	300 μN/s
Hold	60 s	60 s
Unload	10 μN/s	300 μN/s

Note that variations in hardness due to changes in tip geometry during the transition from spherical to conical appear to be comparatively minor for shallow indentations into soft thin films.[25] The results are shown in Fig. 3 and are plotted as a function of the contact radius *a* normalized by the film thickness *t.* Trends in hardness scale with *a*/*t* rather than indentation depth due to the nonideal tip shape. To estimate the hardness of the films, the hardness data (as a function of indenter displacement) were fit using a Bhattacharya and Nix analysis,[12] which has a functional form similar to the experimentally observed hardness trends. Average hardness values used for the substrates were 10 GPa for Si[31,32] and 30 GPa for sapphire.[23] Yield stress was taken as $H_s/3$. The results are shown in Table II along with the mean grain size measured from AFM. The films display an inverse relationship between grain size and hardness similar to other studies on Al thin films.[33,34]

The magnitudes of the hardness values are higher than typically observed for pure aluminum films, which typically range from 0.5 to 1.0 GPa (see for example, Tsui and Pharr[24]). This is most likely due to alloying and grain size effects. Dirks *et al.* have reported up to an 8-fold increase in ultramicrohardness values of 1-μm aluminum alloy films with the addition of up to 10% of a variety of alloying elements.[35] They also reported a 10-fold increase in hardness, from 0.5 to 5 GPa as a result of a decrease in grain size from 1 μm to 30 nm and trapping of plasma gas.

According to the volume fraction models of Burnett and Rickerby[7,8] and Fabes *et al.*,[9] the size of the plastic volumes in the film and substrate determines the hardness. However, the method for determining the volumes differs greatly between the two approaches. Burnett and Rickerby calculate the plastic volumes based on Lawn's formulation of the plastic zone[36] while Fabes *et al.* use a geometric argument. However, Fabes *et al.* still use the volume fraction model, which has the spherical cavity model as its foundation.

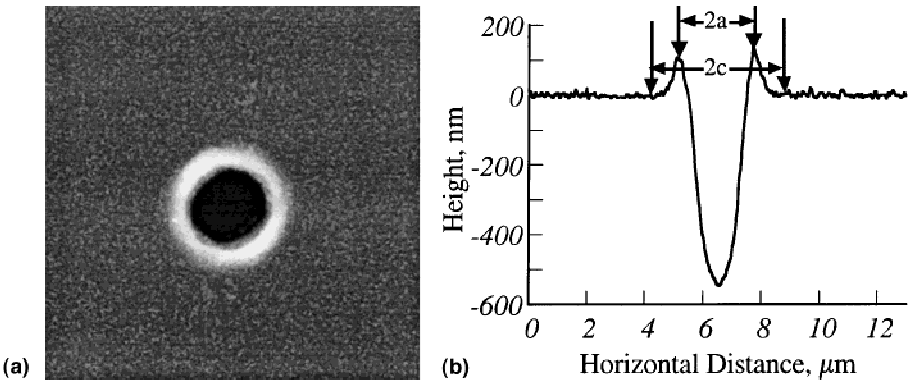

FIG. 2. (a) Plan-view AFM image of an indent into a 500-nm Al–2 wt% Si film on silicon. The scan is 10 × 10 μm. (b) The variation in height along a cross section taken through the center of contact. The arrows mark the extent of plastic pileup.

Figure 4 shows the evolution of the plastic zone radius for the Al–2 wt% Si films on Si substrates plotted against the contact radius to film thickness ratio. At a given a/t, the total penetration depth is greatest in the 2-μm film and the most shallow in the 340 nm film; hence, the thicker the film, the larger the plastic zone for a given a/t.

The geometrical nature of plastic zone evolution in the films can be seen by normalizing the plastic zone size by the film thickness (c/t), in which case all data in Fig. 4 converge into a single data set. This can also be seen by normalizing the plastic zone size by the contact radius (c/a), which also reveals the constraint that the substrate imposes on plastic flow of the film. This is shown in Fig. 5 for all films tested, along with FEM results from Laursen and Simo[20] for 1-μm Al films on Si substrates.

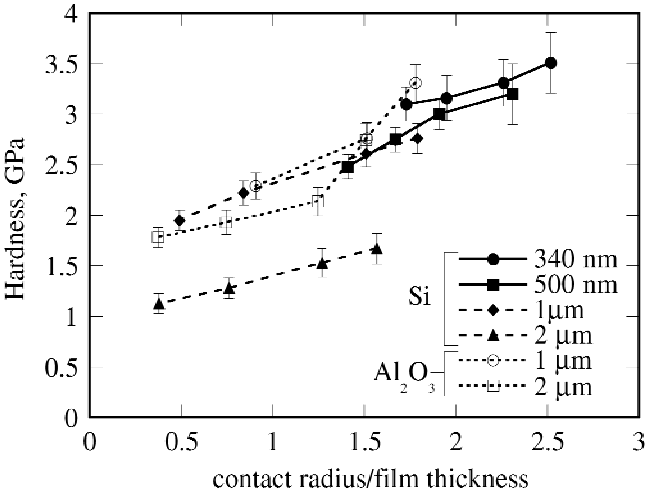

FIG. 3. The variation in composite hardness for Al–2 wt% Si films on silicon and sapphire substrates with increasing contact radius/film thickness. The contact load was measured from the load–displacement data and contact area was measured from the AFM plan-view images. Uncertainty is assessed by systematically measuring inner and outer limits of the contact area.

TABLE II. Hardness for Al–2 wt% Si films as determined by the method of Bhattacharya and Nix[12] along with the approximate grain size as measured by AFM using a line-intercept method. Correlation coefficients are given for the value of H that gives the best curve fit to the data. Uncertainty in grain size is one standard deviation for ten measurements.

Film thickness (μm)	H (GPa)	R^2	Grain size (nm)
Si substrate			
0.34	2.8	0.96	70 ± 10
0.5	2.2	0.94	100 ± 10
1	2.0	0.96	130 ± 30
2	1.0	0.98	220 ± 30
Sapphire substrate			
1	1.9	0.94	140 ± 30
2	1.7	0.88	210 ± 30

For bulk materials, c/a should be constant and independent of penetration depth, but as can be seen, this is not the case for the thin films. The c/a ratio is high for shallow indents (low a/t) and low for deep indents (high a/t). It is recognized that this trend may in part be due to contact area to volume ratio effects, as in the indentation size effect (ISE).[37] However, it is assumed that for an indenter penetration of $a/t > 0.5$ that substrate–film thickness effects dominate any ISE.

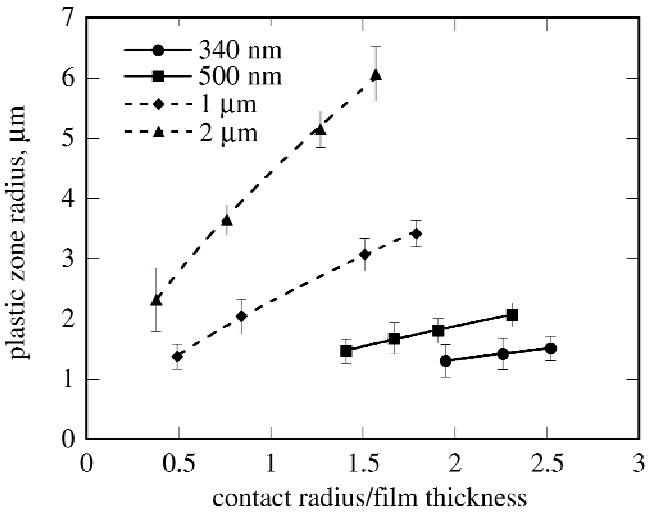

FIG. 4. The evolution of the plastic zone radius as measured from AFM cross sections with increasing penetration depth for Al–2 wt% Si films on silicon substrates. Systematic measurement error is assessed by measuring the inner and outer limits on the plastic zone radius.

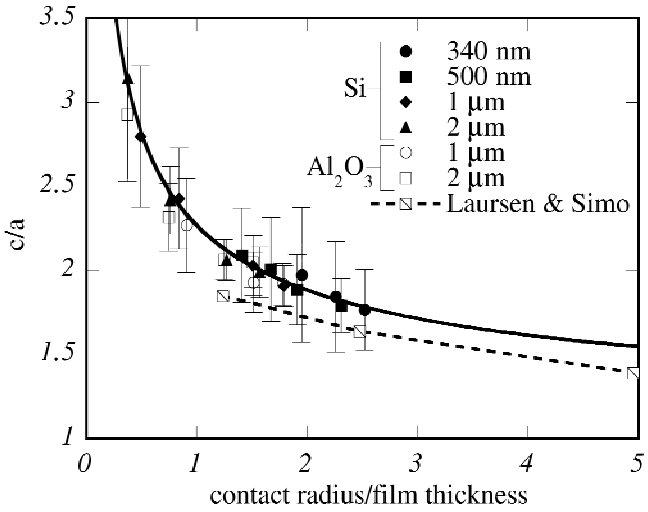

FIG. 5. Evolution of the normalized plastic zone radius for increasing indentation depth for Al–2 wt% Si films on silicon and sapphire substrates. Also shown are the results for FEM calculations by Laursen and Simo[20] for a 136° cone. Uncertainty in contact radius is much less than for the plastic zone radius. Therefore, the uncertainty is given by normalizing the error in the plastic zone measurement by the measured contact radius.

The results of Laursen and Simo[20] follow the same trend as the experimental results, except the *c*/*a* ratio is offset from the experimentally measured values by a constant amount. While within the experimental uncertainty, this may be due to a difference in indenter geometry as the indenter used here is a 90° cone with a 700-nm spherical tip whereas the simulation was conducted using a sharp 136° cone. The decrease in plastic zone radius is symptomatic of the increasing amount of indenter–substrate constraint placed on plastic deformation in the Al–2 wt% Si film.

Of particular interest is the observation that all of the experimentally measured plastic zone radii in Fig. 5 are described by the same curve, independent of the film thickness, film hardness, and substrate modulus. Table II shows there is almost a factor of three difference between the hardness of the 2-μm and 340-nm films, yet no difference between the normalized plastic zone radii. Furthermore, for penetration depths equal to or greater than the film thickness, deformation of the substrate in addition to the film is observed. However, there is little measurable difference between the *c*/*a* ratio for the deepest indents into the 2-μm film or the shallow indents into the 500-nm film. This suggests that the extent of the plastic zone, and by extension the plastic volume, is controlled by the geometry of the contact more so than the elastic–plastic properties of the film or substrate. Note that this would only apply in the case of a soft film and that for deep indents, plastic deformation of the substrate must eventually influence plastic zone development in the film. This also implies that any ISE is second order.

The effects of confinement can also be seen by analyzing the change in total volume for the film–substrate system. This is inferred by measuring the volume of material contained in plastic pileup as well as the volume of the indent impression, which can be calculated from the AFM cross sections according to

$$V = \int_{r_1}^{r_2} 2\pi r h(r) \mathrm{d}r \quad , \tag{2}$$

where r is a distance measured from the center of contact and $h(r)$ is either the height of the pileup or depth of the indent at r. The limits of integration for the contact impression are $r_1 = 0$ to r_2 such that $h(r_2) = 0$, and for the pileup, r_1 such that $h(r_1) = 0$ to $r_2 = c$, the plastic zone radius. The results are shown in Fig. 6, where the ratio of pileup to indent volume is plotted against *a*/*t*. For a rigid-plastic material, $V_{\mathrm{pileup}}/V_{\mathrm{indent}} = 1$, while for a material deforming by radial compression $V_{\mathrm{pileup}}/V_{\mathrm{indent}}$ approaches zero.

Two trends are observed. The first is that the volume ratio tends to, but never reaches the rigid plastic limit with increasing penetration depth. This is due to densification of film porosity, deformation of the Si substrate, and a gradual change of deformation mechanisms in the film. The second trend is that the volume ratio decreases for thinner films. The interpretation here is that substrate–tip interactions play an increasingly important role as the film becomes thinner and that, in line with the *c*/*a* measurements, constraint of the film is increased. A consequence of this increase in constraint is an inability of the film to "squeeze" out from between the indenter and substrate or alternatively, for the indenter to completely penetrate the film. This argument is supported by observations on sectioned indents of GaAs–AlAs heterostructures, which show that the film remains trapped between the indenter and substrate even for penetration depths well beyond the film thickness.[38] Therefore, strain compatibility dictates that further development of plastic strain in the film is determined by the elastic and plastic strains in the substrate.

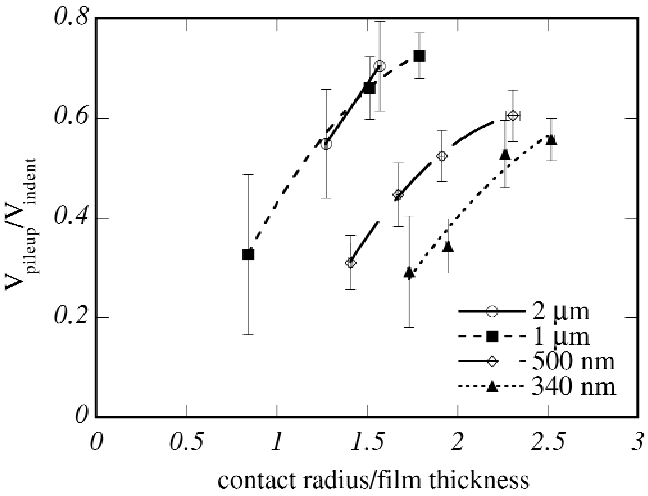

FIG. 6. Ratio of the volume of material contained in the plastic pileup surrounding a contact to the volume of the cavity created by the indent. All films are deposited on a silicon substrate with a thermally grown silicon oxide. Measurement errors are one standard deviation.

B. Geometric model for indentation of soft metal films

The AFM results suggest that deformation of soft films is determined by the geometry of the indenter–substrate contact. The greater the contact radius to film thickness ratio, the greater the constraint on the film under the indenter, and the more restricted plasticity in the film becomes. At shallow indentation depths, there is no restriction on plastic flow in the film and the plastic zone reaches its full extent. As the indentation depth increases, the state of stress in the film underneath the indenter becomes increasingly hydrostatic, such that a core region of the film at the center of contact no longer satisfies the yield criterion. This is a consequence of the compatibility imposed by the substrate, the hydrostatic zone associated with the contact (present in both slip line and spherical cavity models), and an interaction between the two. At

this point, contact pressure begins to rise. As the depth of penetration increases, the confined core region expands and the contact pressure continues to increase until penetration of the substrate begins. Based on the experimental AFM observations and the above outlined approach to the indentation process, a model for determining indentation hardness of soft thin films can be developed.

During the initial stage of contact between an indenter and a soft film, there is negligible interaction with the substrate and as such, the plastic zone is fully developed. This is stage I in the method outlined by Fabes *et al.*[9] At a critical depth, the plastic zone reaches the interface. Figure 5 indicates that $c/a \approx 3$ when $a/t = 1/3$. The indentation depth at which this condition is satisfied is the critical depth δ_{cr}, at which substrate effects begin to occur for a hemispherical plastic zone. Beyond this depth, a core of material at the center of contact arises that may support a higher contact pressure, while the remaining annulus is free to yield. This is shown schematically in Fig. 7. Under this condition, the total load can be written as

$$P = \int_0^{a_{cr}} p_{cr} 2\pi a da + \int_{a_{cr}}^{a} p_m 2\pi a da \quad , \tag{3}$$

where a_{cr} is the radius of the core region, a is the contact radius, p_{cr} is the pressure within the core, and p_m is the mean contact pressure supported by the unconstrained film. The distribution of the pressure within the core is unknown. However, a similar load response will result from a mean contact pressure within the core, $p_{cr\text{-}m}$. Along with a substitution of film hardness H_f for p_m integration of Eq. (3) yields

$$P = \pi a_{cr}^2 (p_{cr\text{-}m} - H_f) + \pi a^2 H_f \quad . \tag{4}$$

The evolution of the core contact radius is calculated by realizing that $c/a \approx 3$ up to the indentation depth at which the core develops ($a_{cr} = 0$). Beyond this depth, material at the center of the contact is constrained, but the surrounding annulus continues to deform under contact pressures representative of the film hardness. The deformation in this annulus results in further expansion of the plastic zone in a geometrical fashion similar to the relationship between contact radius and plastic zone size for low indentation depths. This can be expressed as

$$\frac{c - a_{cr}}{a - a_{cr}} = 3 \quad ,$$

which can be rearranged to give an expression for a_{cr},

$$a_{cr} = \frac{a}{2}\left(3 - \frac{c}{a}\right) \quad . \tag{5}$$

Thus, the core radius can be calculated from experimentally measured quantities.

An expression is also needed for the evolution of the contact pressure within the core region. At the first instant when the core region appears, the pressure in the core is equal to H_f. This happens at a penetration depth of δ_{cr}, such that $a/t \approx 1/3$, (see the above discussion). The mean contact pressure in the core region, $p_{cr\text{-}m}$, rises continuously until the indentation depth exceeds the film thickness. At this depth, deformation of the substrate is induced and the contact pressure within a small area under the indenter rises to the substrate hardness H_s. The maximum contact pressure within the core $p_{cr\text{-}max}$, is a strong function of tip shape, and has an upper bound of H_s, although it does not have to rise to the value of H_s. By allowing $p_{cr\text{-}m}$ to vary in a linear fashion with indentation depth δ up to a maximum value of

$$p_{cr\text{-}m} = \frac{p_{cr\text{-}max} + H_f}{2} \quad ,$$

for indentation depths equal to the film thicness t the mean contact pressure within the core region can be given as follows:

$$p_{cr\text{-}m}(\delta,t) = \frac{p_{cr\text{-}max} - H_f}{2(1 - \delta_{cr}/t)}\left(\frac{\delta}{t} - 1\right) + \frac{p_{cr\text{-}max} + H_f}{2} \quad . \tag{6}$$

Due to the sphero-conical shape of the indenter, δ/t is a function of contact area and film thickness [$\delta/t = f(a/t, t)$]. Thus, $\delta_{cr/t}$ and the functional form of δ/t are calculated from measured values of a, c, and δ for each film thickness. Substituting Eqs. (5) and (6) into Eq. (4) gives an expression for hardness in terms of contact area:

$$H_c = \frac{1}{4}\left(3 - \frac{c}{a}\right)^2 \left\{\frac{p_{cr\text{-}max} - H_f}{2(1 - \delta_{cr}/t)}\left[f(a/t,t) - 1\right] + \frac{p_{cr\text{-}max} + H_f}{2}\right\} + H_f \quad . \tag{7}$$

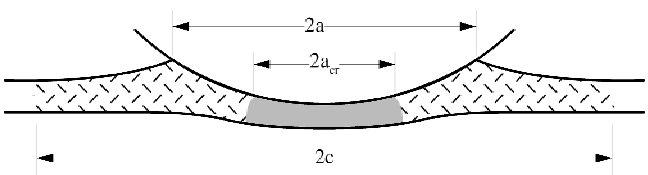

FIG. 7. A schematic representation of the evolution of the plastic zone in the aluminum film. The lightly shaded region is free to plastically deform while the darker shaded region is increasingly under a state of hydrostatic stress and experiences a higher contact pressure than the rest of the contact. The radius of this region is denoted a_{cr}.

Finally, the evolution of *c/a* is determined based on Fig. 5, realizing the *c/a* cannot be less than 1, by fitting the data to an equation of the form:

$$\frac{c}{a} = 1 + C_1\left(\frac{a}{t}\right)^n; \text{ for } a/t > 1/3 \quad . \tag{8}$$

C_1 and n are fitting parameters and give a best fit to the data for $C_1 = 1.27$ and $n = -0.5$.

This model has a different form compared to other formulations of composite hardness[13] but is analogous to the area fraction model.[4] Although the plastic zone is involved in this calculation, it is used only to determine the level of constraint imposed on the film trapped between the indenter and the substrate. It is not used to calculate plastic volumes, as discussed by Ford.[18] The level of constraint is incorporated into the model through the radius of the core capable of supporting an elevated contact pressure.

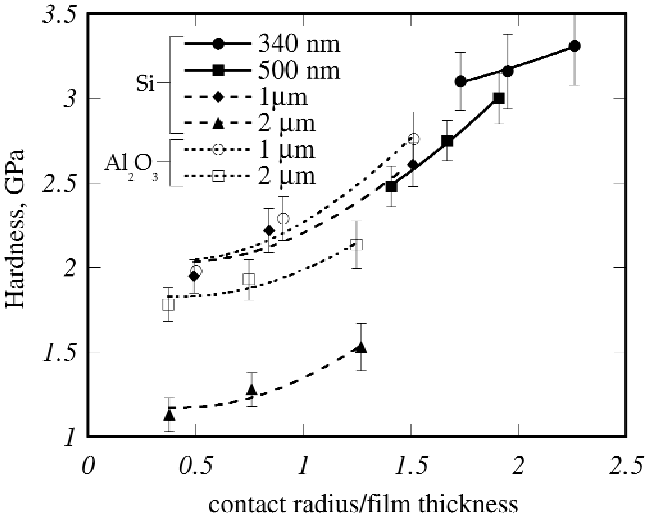

FIG. 8. The best fit to the hardness data according to the constrained plastic zone core model of Eq. (7) for the Al–2 wt% Si films on thermally oxidized silicon and sapphire substrates. Substrate and film thickness data are given in the legend. The hardness values for the film and substrate are listed in Table III.

TABLE III. Best fit H_f and $p_{cr\text{-}max}$ hardness values according to Eq. (7) for both oxidized silicon and sapphire substrates. Correlation coefficients are given for the values giving the best fit. The hardness of the Al–2 wt% Si films according to the method of Bhattacharya and Nix are also presented for comparison.[12] For the purposes of that analysis, the hardness of the oxidized Si was taken to be 10 GPa, while the hardness of the sapphire was 30 GPa.

Film thickness (μm)	H_f (GPa)	$p_{cr\text{-}max}$ (GPa)	R^2	$H_{B\text{-}N}$ (GPa)
Si substrate				
0.34	2.9	5.3	0.99	2.8
0.5	2.1	8.3	0.99	2.2
1	2.0	7.0	0.96	2.0
2	1.2	5.1	0.97	1.0
Sapphire substrate				
1	2.0	8.5	0.98	1.9
2	1.8	5.4	0.96	1.7

For the indentations in this experiment, the substrate either remained elastic or experienced small levels of plastic strain. For deep indentations, or softer substrates, the plastic zone size of the substrate would be on the same order as or larger than that of the film. In such a case, AFM measurements would not be representative of the size of the plastic zone of the film, nor would the model apply to those situations. Note that the model might be extended to penetration depths greater than the film thickness by addition of a region within the contact area for which the contact pressure is that of the substrate hardness, H_s. However, this has not been attempted here. Consequently, indentation depths greater than the film thickness have been excluded when applying the model.

Figure 8 shows the best fit to the hardness data for the Al–2 wt% Si on silicon and sapphire substrates using Eq. (7) with H_f and $p_{cr\text{-}max}$ as fitting parameters. Table III lists those values of H_f and $p_{cr\text{-}max}$ with H_f values determined from the Bhattacharya and Nix analysis.[12] The results for the film hardness compare quite favorably. Note that the maximum contact pressure within the core region $p_{cr\text{-}max}$ is similar for the same film thickness on either substrate and that it approaches but does not reach the value of the substrate hardness in either system (10 GPa for Si[37,38] and 30 GPa for sapphire[23]). With the exception of the 340-nm film on Si, it also increases with decreasing film thickness.

Film hardness, according to Eq. (7), is not particularly sensitive to systematic measurement errors. Assuming the plastic zone measurements are underestimated by 10% results in statistically insignificant increases in film hardness. However, $p_{cr\text{-}max}$ shows significant sensitivity to such an underestimation, with pressures increasing from 10% to 25%. The value of $p_{cr\text{-}max}$ is even more sensitive to the choice of contact radius at which the plastic zone radius reaches the film–substrate interface. A decrease in the critical *c*/*a* value from 3 to 2.7 increases the substrate hardness by 25% to 50%.

IV. CONCLUSIONS

AFM was used to investigate the evolution of the plastic zone for thin Al–2 wt% Si films on silicon and sapphire substrates. It was found that regardless of the substrate properties, hardness of the film, or film thickness, the ratio of plastic zone radius to contact radius assumes a single value at a given *a*/*t*. The decrease in *c*/*a* provides a measure of the constraint of the film within the contact. This observation has been combined with a simple model that partitions the hardness between a core region that supports a higher contact pressure and an

annulus of material that supports a pressure equal to the hardness of the film. The model was used to successfully calculate the hardness of Al–2 wt% Si films on silicon and sapphire substrates.

Trends in the pileup to indent volume ratio were also explored as a function of film thickness and penetration depth. It was found that the volume ratio approaches, but does not reach unity for thicker films and deeper indentation depths. Possible mechanisms for this behavior include a switch from radial compression to a slip-line type mechanism. With decreasing film thickness, the indentation volume is increasingly determined by substrate deformation and thin film constraint.

ACKNOWLEDGMENTS

The authors would like to thank J.A. Schneider, formerly of Sandia National Laboratories and currently at Mississippi State University, for performing the x-ray diffraction experiments. D.E.K. and N.R.M. gratefully acknowledge the support of the United States Department of Energy (U.S. DOE) under Contract No. DE-AC04-94AL85000. W.W.G. and A.A.V. gratefully acknowledge the support of the Center for Interfacial Engineering at the University of Minnesota under Grant No. NSF/CDR-8721551 and the U.S. DOE under Contract No. DE-FG02/96ER45574.

Identification of commercial equipment does not imply recommendation or endorsement by NIST.

REFERENCES

1. D. Lebouvier, P. Gilormini, and E. Felder, J. Phys. D **18,** 199 (1985).
2. A.K. Bhattacharya and W.D. Nix, Int. J. Sol. Struct. **27,** 1047 (1991).
3. D. Lebouvier, P. Gilormini, and E. Felder, Thin Solid Films **172,** 227 (1989).
4. B. Jönsson and S. Hogmark, Thin Solid Films **114,** 257 (1984).
5. P.M. Sargent, in *Microindentation Techniques in Materials Science,* ASTM Spec. Tech. Publ. 889, edited by P.J. Blau and B.R. Lawn (ASTM, Philadelphia, PA, 1986).
6. P.J. Burnett and T.F. Page, J. Mater. Sci. **19,** 845 (1984).
7. P.J. Burnett and D.S. Rickerby, Thin Solid Films **148,** 41 (1987).
8. P.J. Burnett and D.S. Rickerby, Thin Solid Films **148,** 51 (1987).
9. B.D. Fabes, W.C. Oliver, R.A. McKee, and F.J. Walker, J. Mater. Res. **7,** 3056 (1992).
10. J-H. Ahn and D. Kwon, J. Appl. Phys. **82,** 3266 (1997).
11. D. Stone, W.R. LaFontaine, P. Alexopoulos, T-W. Wu, and C-Y. Li, J. Mater. Res. **3,** 141 (1988).
12. A.K. Bhattacharya and W.D. Nix, Int. J. Sol. Struct. **24,** 1287 (1988).
13. M. Wittling, A. Bendavid, P.J. Martin, and M.V. Swain, Thin Solid Films **270,** 283 (1995).
14. R. Hill, *The Mathematical Theory of Plasticity* (Clarendon Press, Oxford, United Kingdom, 1950).
15. D.M. Marsh, Proc. R. Soc. London **A279,** 420 (1964).
16. K.L. Johnson, J. Mech. Phys. Sol. **18,** 115 (1970).
17. S.S. Chiang, D.B. Marshall, and A.G. Evans, J. Appl. Phys. **53,** 298 (1982).
18. I.J. Ford, Thin Solid Films **245,** 122 (1994).
19. F.E. Kennedy and F.F. Ling, J. Eng. Mater. Tech. **86,** 97 (1974).
20. T.A. Laursen and J.C. Simo, J. Mater. Res. **7,** 618 (1992).
21. A. Bolshakov and G.M. Pharr, J. Mater. Res. **13,** 1049 (1998).
22. M.F. Doerner and W.D. Nix, J. Mater. Res. **1,** 601 (1986).
23. W.C. Oliver and G.M. Pharr, J. Mater. Res. **7,** 1564 (1992).
24. T.Y. Tsui and G.M. Pharr, J. Mater. Res. **14,** 292 (1999).
25. C-J. Lu and D.B. Bogy, Int. J. Solids Struct. **32,** 1759 (1995).
26. S. Harvey, H. Huang, S. Venkataraman, and W.W. Gerberich, J. Mater. Res. **8,** 1291 (1993).
27. D. Kramer, H. Huang, M. Kriese, J. Robach, J. Nelson, A. Wright, D. Bahr, and W.W. Gerberich, Acta Mater. **47,** 333 (1999).
28. W. Zielinski, H. Huang, and W.W. Gerberich, J. Mater. Res. **8,** 1300 (1993).
29. W. Zielinski, H. Huang, S. Venkataraman, and W.W. Gerberich, Phil. Mag. A **72,** 1221 (1995).
30. L.E. Samuels and T.O. Mulhearn, J. Mech. Phys. Solids **5,** 125 (1957).
31. T.F. Page, W.C. Oliver, and C.J. McHargue, J. Mater. Res. **7,** 450 (1992).
32. G.M. Pharr, W.C. Oliver, R.F. Cook, P.D. Kirchner, M.C. Kroll, T.R. Dinger, and D.R. Clarke, J. Mater. Res. **7,** 961 (1992).
33. M.F. Doerner, D.S. Gardner, and W.D. Nix, J. Mater. Res. **1,** 845 (1986).
34. R. Venkatraman and J.C. Bravman, J. Mater. Res. **7,** 2040 (1992).
35. A.G. Dirks, P.E. Wierenga, and J.J. van den Broek, Thin Solid Films **172,** 51 (1989).
36. B.R. Lawn, A.G. Evans, and D.B. Marshall, J. Am. Ceram. Soc. **63,** 574 (1980).
37. M.I. Baskes (private communication, Los Alamos National Laboratories, 1999).
38. M.R. Castell, G. Shafirstein, and D.A. Ritchie, Philos. Mag. A **74,** 1185 (1996).